Photochemical Evolution of the 2013 California Rim Fire: Synergistic Impacts of Reactive Hydrocarbons and Enhanced Oxidants

Glenn M. Wolfe[1], Thomas F. Hanisco[1], Heather L. Arkinson[2], Donald R. Blake[3], Armin Wisthaler[4,5], Tomas Mikoviny[5], Thomas B. Ryerson[6,7,*], Ilana Pollack[7,**], Jeff Peischl[7], Paul O. Wennberg[8,9], John D. Crounse[8], Jason M. St. Clair[8,***], Alex Teng[8,****], L. Greg Huey[10], Xiaoxi Liu[10,*****], Alan Fried[11], Petter Weibring[11], Dirk Richter[11], James Walega[11], Samuel R. Hall[12], Kirk Ullmann[12], Jose L. Jimenez[7,13], Pedro Campuzano-Jost[7,13], T. Paul Bui[14], Glenn Diskin[15], James R. Podolske[14], Glen Sachse[15,16,†], and Ronald C. Cohen[17,18]

[1]Atmospheric Chemistry and Dynamics Laboratory, NASA Goddard Space Flight Center, Greenbelt, MD, USA
[2]Department of Oceanic and Atmospheric Science, University of Maryland, College Park, MD, USA
[3]Department of Chemistry, University of California Irvine, Irvine, CA, USA
[4]Institute for Ion Physics and Applied Physics, University of Innsbruck, Innsbruck, Austria
[5]Department of Chemistry, University of Oslo, Oslo, Norway
[6]Chemical Sciences Laboratory, NOAA, Boulder, CO, USA
[7]Cooperative Institute for Research in Environmental Sciences, University of Colorado Boulder, Boulder, CO, USA
[8]Division of Geological and Planetary Sciences, California Institute of Technology, Pasadena, CA, USA
[9]Division of Engineering and Applied Science, California Institute of Technology, Pasadena, CA, USA
[10]School of Earth and Atmospheric Sciences, Georgia Institute of Technology, Atlanta, GA, USA
[11]Institute of Arctic and Alpine Research, University of Colorado, Boulder, CO, USA
[12]Atmospheric Chemistry Observations and Modeling Laboratory, National Center for Atmospheric Research, Boulder, CO, USA
[13]Department of Chemistry, University of Colorado Boulder, Boulder, CO, USA
[14]Atmsopheric Sciences Branch, NASA Ames Research Center, Moffett Field, CA, USA
[15]NASA Langley Research Center, Hampton, VA, USA
[16]National Institute of Aerospace, Hampton, VA, USA
[17]Department of Earth and Planetary Sciences, University of California, Berkeley, CA, USA
[18]College of Chemistry, University of California, Berkeley, CA, USA
[*]Now at Scientific Aviation, Boulder, CO, USA
[**]Now at Department of Atmospheric Science, Colorado State University, Fort Collins, CO, USA
[***]Now at Joint Center for Earth Systems Technology, University of Maryland Baltimore County, Baltimore, MD, USA
[****]Now at Fifty Years, San Francisco, CA, USA
[*****]Now at California Air Resource Board, Los Angeles, CA, USA
[†]Deceased

Text S1. Adjustment of Lab-Reported ERs

As noted in Sect. 2.4 of the main text, we adjust the emission ratios of acrolein and biacetyl downward by factors of 2.3 and 10, respectively, relative to the values reported by Koss et al. (2018). Here we provide some justification for these modifications.

For acrolein, instrument inter-comparisons during and after FIREX-AQ recently revealed a factor of 2.3 error in the quantification of the NOAA acrolein gas standard (personal communication, A. Wisthaler and M. Coggon, 2021). This is the same standard used in Koss et al. (2018).

For biacetyl (2,3-butanedione), it is likely that the work of Koss et al. (2018) did not account for all potential isomers in the PTR-ToF-MS interpretation. The molecular formula for this compound is $C_4H_6O_2$. Using GC-CIMS data, Koss et al. (2018) inferred contributions to this PTR-ToF-MS signal from biacetyl (87%), methacrylate (5%), and other unidentified compounds (8%). Previous work has suggested the presence of additional isomers that are not easily detected by GC. In one study of pine burning emissions, 2-oxobutanal emissions were 3 times greater than those of biacetyl (Schauer et al., 2001). 1,4-butanedial has also been observed in significant amounts in tobacco smoke (personal communication, A. Wisthaler, 2021). Based on the likely presence of these compounds, we conservatively reduce biacetyl by a factor of 10.

These adjustments reduce model over-prediction for APAN (produced solely from acrolein oxidation) and PAN (where biacetyl is a major precursor) in sensitivity simulations described in the main text.

Text S2. Other oVOC

Figure S13 shows the age progression of several other oVOC. Methanol is long-lived, and variability may reflect changing emissions or background conditions (Fig. S13a). A sharp rise in the methanol NEMR at 2 h may be another indicator of biogenic influence. Acetone and propanal are isomers (C_3H_6O) and are reported as a sum in the SEAC^{4}RS dataset. Acetone is likely the dominant isomer given the short lifetime of propanal, and this is consistent with the small NEMR variability as the lifetime of acetone against oxidation is weeks (Fig. S13b). The hydroxyacetone NEMR is relatively constant with age, and model values agree with observations within uncertainties (Fig. S13c). The sum of MVK and MACR tells a story similar to acetaldehyde, with a biogenic signature at ~2 h and an over-rapid decline in the base simulation (Fig S13d). Results from other simulations are discussed in the main text, when relevant.

Text S3. Additional NO_y Details

Several studies have noted potential positive artifacts in NO_2 measurements due to decomposition of thermally unstable gases in the sample inlet or instrument (Browne et al., 2011; Silvern et al., 2018; Nault et al., 2015). This is unlikely to explain the discrepancy between observed and modeled NO_x in simulations M0 and M1 (Fig. 2i) for several reasons. First, such an interference would need to affect both the TDLIF and chemiluminescence NO_2 measurements similarly, as these two measurements are strongly correlated: NO_2(TDLIF) = 1.2*NO_2(CL) – 0.12 ppbv, r^2 = 1.00. Second, if the artifact were due to known NO_x reservoirs, the conversion efficiency would need to be substantial. The difference between observed and modeled NO_2 in simulation M1 is 260 $\pm$ 100 pptv at ages beyond 5 h. Mean observed PAN and total PNs are 1.3 and 2.1 ppbv, respectively. Thus a conversion efficiency of 10% or more would be required to fully explain the model-measurement difference, and this is unlikely given typical aircraft cabin and inlet temperatures (< 40 °C). Modeled HO_2NO_2 and $CH_3O_2NO_2$ are < 5 pptv and < 1 pptv, respectively. We cannot rule out the potential influence of yet-unidentified NO_x reservoirs, though previous work suggests such artifacts are likely limited to the upper troposphere (Silvern et al., 2018).

In addition to PAN (discussed in the main text), the SEAC^{4}RS dataset includes observations of several other speciated peroxy nitrates (PNs) and a total PN measurement. Other speciated PNs, shown in Fig. S14, include peroxypropionyl nitrate (PPN), peroxyacryloyl nitrate (APAN), and peroxyisobutyryl nitrate (PiBN). In the base simulation, early PPN NEMR growth is under-predicted, but the model and observations converge after 2h. APAN and PiBN are generally under-predicted, due in part to a lack of VOC precursors in the base simulation. Changes in model PNs in simulation M1 reflect increases in VOC precursors. In particular, APAN is produced solely through oxidation of acrolein. All PNs increase upon addition of initial HONO or pNO_3^- photolysis due to more RO_2 and NO_2. Conversely, heterogeneous NO_2 conversion to HONO has essentially no effect on PN NEMRs. In this case, decreasing NO_2 and increasing NO offsets the increase in RO_2.

Model-measurement comparison with the ΣPN observations tell a qualitatively similar story to the speciated data (Fig. S15a). This measurement (via thermal dissociation and laser-induced fluorescence detection of NO_2) is typically higher than the sum of speciated PN measurements (via thermal dissociation and detection of the peroxyacyl radicals), and in the first few hours this difference exceeds the combined uncertainty of the measurements. The reasons for this difference are unclear.

Alkyl nitrates (ANs) are minor products of the reaction of organic peroxy radicals (RO_2) with NO. The observed ΣAN NEMR is variable with no clear trend (Fig. S15b). The simulated ΣAN NEMR is relatively constant throughout each simulation, and all simulations fall within the variability of observed NEMRs.

References

Akagi, S. K., Yokelson, R. J., Wiedinmyer, C., Alvarado, M. J., Reid, J. S., Karl, T., Crounse, J. D., and Wennberg, P. O.: Emission factors for open and domestic biomass burning for use in atmospheric models, 11, 4039–4072, https://doi.org/10.5194/acp-11-4039-2011, 2011.

Browne, E. C., Perring, A. E., Wooldridge, P. J., Apel, E., Hall, S. R., Huey, L. G., Mao, J., Spencer, K. M., Clair, J. M. S., Weinheimer, A. J., Wisthaler, A., and Cohen, R. C.: Global and regional effects of the photochemistry of $CH_3O_2NO_2$: evidence from ARCTAS, 11, 4209–4219, https://doi.org/10.5194/acp-11-4209-2011, 2011.

Gustafson, W. and Yu, S.: Generalized approach for using unbiased symmetric metrics with negative values: normalized mean bias factor and normalized mean absolute error factor, 13, 262–267, https://doi.org/10.1002/asl.393, 2012.

Koss, A. R., Sekimoto, K., Gilman, J. B., Selimovic, V., Coggon, M. M., Zarzana, K. J., Yuan, B., Lerner, B. M., Brown, S. S., Jimenez, J. L., Krechmer, J., Roberts, J. M., Warneke, C., Yokelson, R. J., and de Gouw, J.: Non-methane organic gas emissions from biomass burning: identification, quantification, and emission factors from PTR-ToF during the FIREX 2016 laboratory experiment, 18, 3299–3319, https://doi.org/10.5194/acp-18-3299-2018, 2018.

Nault, B. A., Garland, C., Pusede, S. E., Wooldridge, P. J., Ullmann, K., Hall, S. R., and Cohen, R. C.: Measurements of CH3O2NO2 in the upper troposphere, 987–997, https://doi.org/10.5194/amt-8-987-2015, 2015.

Schauer, J. J., Kleeman, M. J., Cass, G. R., and Simoneit, B. R. T.: Measurement of Emissions from Air Pollution Sources. 3. C1−C29 Organic Compounds from Fireplace Combustion of Wood, Environ. Sci. Technol., 35, 1716–1728, https://doi.org/10.1021/es001331e, 2001.

Silvern, R. F., Jacob, D. J., Travis, K. R., Sherwen, T., Evans, M. J., Cohen, R. C., Laughner, J. L., Hall, S. R., Ullmann, K., Crounse, J. D., Wennberg, P. O., Peischl, J., and Pollack, I. B.: Observed NO/NO2 Ratios in the Upper Troposphere Imply Errors in NO-NO2-O3 Cycling Kinetics or an Unaccounted NOx Reservoir, 45, 4466–4474, https://doi.org/10.1029/2018GL077728, 2018.

Toon, O. B., Maring, H., Dibb, J., Ferrare, R., Jacob, D. J., Jensen, E. J., Luo, Z. J., Mace, G. G., Pan, L. L., Pfister, L., Rosenlof, K. H., Redemann, J., Reid, J. S., Singh, H. B., Thompson, A. M., Yokelson, R., Minnis, P., Chen, G., Jucks, K. W., and Pszenny, A.: Planning, implementation, and scientific goals of the Studies of Emissions and Atmospheric Composition, Clouds and Climate Coupling by Regional Surveys (SEAC(4)RS) field mission, 121, 4967–5009, https://doi.org/10.1002/2015JD024297, 2016.

Table S1. SEAC^{4}RS measurement details.

Measurement	Instrument[a]	Accuracy
Pressure Temperature	MMS	< 1%
H_2O	DLH	5%
Photolysis frequencies	CAFS	12 – 20%[b]
O_3 NO NO_2 NO_2	NOyO3 TDLIF	3% 4% 7% 5%
H_2O_2 HNO_3 HCN Peroxyacetic acid Hydroxyacetone Hydroxymethyl hydroperoxide Ethene hydroxynitrate Propene hydroxynitrate Butene hydroxynitrate Ethanal nitrate Propanone nitrate Isoprene hydroxynitrate	CIT-CIMS	30% 30% 50% 50% 40% 50% 50% 30% 50% 50% 50% 30%
CO	DACOM	2%
PAN PPN APAN PiBN	GT-CIMS	15% 20% 40% 40%
ΣPN ΣAN	TDLIF	10% 15%
Particulate nitrate	AMS	17%
VOC[c]	WAS	5%
CH_3CN CH_3OH CH_3CHO Acetone + propanal MVK + MACR Isoprene + Furan Methanol	PTR-MS	15% 15% 15% 5% 10% 5% 15%
HCHO	ISAF CAMS	10% 4%
Aerosol surface area	LAS	20%
Solar irradiance	BBR	5%

[a]See Toon et al. (2016) for details and references.
[b]Varies based on uncertainties in recommended cross sections and quantum yields.
[c]Methyl nitrate, ethyl nitrate, isopropyl nitrate, n-propyl nitrate, 2-butyl nitrate, 3-methyl-2-butyl nitrate, 3-pentyl nitrate, 2-pentyl nitrate, methane, ethane, propane, n-butane, isobutene, n-pentane,

isopentane, n-hexane, 2-methyl pentane, 3-methyl pentane, 2,3-dimethylbutane, n-heptane, ethene, propene, 1-butene, cis-2-butene, trans-2-butene, isobutene, 1,3-butadiene, 1-pentene, propadiene, benzene, toluene, ethyl benzene, o-xylene, m-xylene + p xylene (measured as sum, assumed 50%/50% distribution), isoprene, α-pinene, β-pinene.

Table S2. MCM assignments for unmeasured VOC.

Koss ID	Koss Formula	MCM Name	Emission Ratio (ΔX/ΔCO)
Species with direct MCM analogues			
Acetic acid + glycolaldehyde	C2H4O2H	CH3CO2H	10.7633
Acetic acid + glycolaldehyde	C2H4O2H	HOCH2CHO	5.3013
HONO	HNO2H	HONO	3.2765
2-furfural + 3-furfural + other HCO2	C5H4O2H	FURFURAL2	3.2625
Formic acid	CH2O2H	HCOOH	2.3024
2-(3H)Furanone	C4H4O2H	BZFUONE	1.8951
5-Methyl furfural +Benzene diols (=catechol, resorcinol)	C6H6O2H	MFURFURAL	1.8749
5-Methyl furfural +Benzene diols (=catechol, resorcinol)	C6H6O2H	CATECHOL	1.8749
Guaiacol (=2-methoxyphenol)	C7H8O2H	GUAIACOL	1.8696
Acrolein	C3H4OH	ACR	1.8446
2-Methylphenol (=o-cresol) + anisol	C7H8OH	CRESOL	1.7222
Phenol	C6H6OH	PHENOL	1.7124
2-Methoxy-4-methylphenol (= creosol)	C8H10O2H	MGUAIACOL	1.1605
2-methylfuran + 3-methylfuran + general HCO	C5H6OH	M2F	0.9074
methyl acetate + ethyl formate + hydroxyacetone	C3H6O2H	METHACET	0.9060
Pyruvaldehyde (=methyl glyoxal) + acrylic acid	C3H4O2H	MGLYOX	0.7083
Pyruvaldehyde (=methyl glyoxal) + acrylic acid	C3H4O2H	ACO2H	0.7083
Glyoxal	C2H2O2H	GLYOX	0.7048
MEK + butanal + 2-methylpropanal	C4H8OH	MEK	0.5282
MVK + methacrolein + crotonaldehyde	C4H6OH	C4ALDB	0.5053
Quinone (=p-Benzoquinone)	C6H4O2H	PBZQONE	0.4795
Ethanol	C2H6OH	C2H5OH	0.4481
2,5-dimethyl furan + 2-ethylfuran + other C2 substituted furans	C6H8OH	DIM25FURAN	0.4226
C2 Phenols + methyl anisol	C8H10OH	OXYLOL	0.4222
methyl acetate + ethyl formate + hydroxyacetone	C3H6O2H	ETHFORM	0.3624
Acetic anhydride	C4H6O3H	METHCOACET	0.3198
Benzaldehyde	C7H6OH	BENZAL	0.1962
2-methylfuran + 3-methylfuran + general HCO	C5H6OH	M3F	0.1779
2,3-butanedione + methyl acrylate + other HCO2	C4H6O2H	BIACET	0.1650
Styrene	C8H8H	STYRENE	0.1625
2-furfural + 3-furfural + other HCO2	C5H4O2H	FURFURAL3	0.1554
syringol	C8H10O3H	SYRINGOL	0.1485
Tolualdehyde	C8H8OH	PXYLAL	0.0900
Tolualdehyde	C8H8OH	MXYLAL	0.0900
3-methyl-2-butanone + 2-methylbutanal+3-methylbutanal+2-pentanone +3-pentanone	C5H10OH	MIPK	0.0877

MEK + butanal + 2-methylpropanal	C4H8OH	IPRCHO	0.0870
Tolualdehyde	C8H8OH	OXYLAL	0.0772
3-methyl-2-butanone + 2-methylbutanal+3-methylbutanal+2-pentanone +3-pentanone	C5H10OH	MPRK	0.0653
Methyl benzoic acid	C8H8O2H	PXYLCO2H	0.0652
Methyl benzoic acid	C8H8O2H	MXYLCO2H	0.0652
Sesquiterpenes	C15H24H	BCARY	0.0651
Methyl benzoic acid	C8H8O2H	OXYLCO2H	0.0559
3-methyl-2-butanone + 2-methylbutanal+3-methylbutanal+2-pentanone +3-pentanone	C5H10OH	DIEK	0.0428
Pyruvic acid	C3H4O3H	CH3COCO2H	0.0407
heptanal + 2,4-dimethyl-3-pentanone + heptanone	C7H14OH	C6H13CHO	0.0317
heptanal + 2,4-dimethyl-3-pentanone + heptanone	C7H14OH	HEPT3ONE	0.0186
Dimethyl sulfide	C2H6SH	DMS	0.0116
hexanal + hexanones	C6H12OH	C5H11CHO	0.0110
hexanal + hexanones	C6H12OH	HEX2ONE	0.0070
MEK + butanal + 2-methylpropanal	C4H8OH	C3H7CHO	0.0062
hexanal + hexanones	C6H12OH	HEX3ONE	0.0054
3-methyl-2-butanone + 2-methylbutanal+3-methylbutanal+2-pentanone +3-pentanone	C5H10OH	BUT2CHO	0.0041
3-methyl-2-butanone + 2-methylbutanal+3-methylbutanal+2-pentanone +3-pentanone	C5H10OH	C3ME3CHO	0.0041
Species mapped to MCM using OH reaction rate coefficient and molecular formula			
2-furanmethanol + other HCO2	C5H6O2H	MEKAOH	1.7325
5-(hydroxymethyl)-2-furfural	C6H6O3H	C512OOH	1.0774
5-hydroxymethyl-2[3H]-furanone	C5H6O3H	C512OOH	0.9055
2-hydroxy-3-methyl-2-cyclopenten-1-one	C6H8O2H	HEX3ONDOOH	0.7753
Product of levoglucosan dehydration (pyrolysis)	C6H8O4H	M3HEXANO3	0.6436
2,5-di(hydroxymethyl)furan + Methyl hydroxy dihydrofurfural	C6H8O3H	CO1M22CHO	0.5730
Methyl methacrylate + other HCO2	C5H8O2H	HO2CO4CHO	0.5689
3-methyl-3-butene-2-one + cyclopentanone + HCO1 isomers	C5H8OH	PEBOH	0.5685
5-Hydroxy 2-furfural/2-furoic acid	C5H4O3H	C4DBDIKET	0.4838
2,4-Cyclopentadiene-1-one + 2 other HCO isomers	C5H4OH	HO25C6	0.4779
Vanillin	C8H8O3H	C7CO4EDB	0.4712
Methyl propanoate	C4H8O2H	MAE	0.4602
Vinyl guaiacol	C9H10O2H	LIMKET	0.3705
Acetamide	C2H5NOH	ACO2H	0.3637
5-hydroxymethyl tetrahydro 2-furanone + 5-hydroxy tetrahydro 2-furfural	C5H8O3H	CO2M33CO3H	0.3543
C3 furan + various HCO	C7H10OH	HO25C7	0.3052
1-Buten-3-yne	C4H4H	ACR	0.2894
pyrrole + butene nitrile isomers	C4H5NH	C5H8	0.2417

Eugenol + isoeugenol	C10H12O2H	LIMKET	0.2415
Nitromethane	CH3NO2H		0.2264
2-propynal	C3H2OH	ACR	0.2091
Dihydro furandione	C4H4O3H	HMACO3H	0.2083
Hydroxy benzoquinone	C6H4O3H	M3HEXANO3	0.2058
2-hydroxybenzaldehyde (=Salicylaldehyde)	C7H6O2H	HO3C5CHO	0.1526
Pyridine + pentadienenitriles	C5H5NH	M23C4	0.1432
Naphthalene	C10H8H	UDECOH	0.1388
C9 Aromatics	C9H12H	DECOH	0.1255
methane thiol	CH4SH	CHCL2CHO	0.1243
Methyl benzofuran	C9H8OH	NOPINAOH	0.1191
C6 Diones + C6 1-DBE esters	C6H10O2H	IEB4CHO	0.1141
Acrylonitrile	C3H3NH	DICLETOH	0.1138
Methyl thiophenes	C5H6SH	ETBE	0.1098
1,3-Cyclopentadiene	C5H6H	ME2BUT2ENE	0.1055
dimethylbenzofuran	C10H10OH	NOPINAOH	0.1045
Methyl cyclopentanone + cyclohexanone + other ketones	C6H10OH	M3PECOOH	0.0927
methyl isocyanate + hydroxyacetonitrile	C2H3NOH	ETHOX	0.0871
3-methylacetophenone	C9H10OH	C8BCCO	0.0870
Methyl propenyl benzene + ethyl styrene	C10H12H	C7MOCOCO3H	0.0860
Formamide	CH3NOH	CCL3CHO	0.0842
Indane + methyl styrenes + propenyl benzenes	C9H10H	APINENE	0.0820
Benzofuran	C8H6OH	NOPINAOH	0.0819
Propane nitrile	C3H5NH	CH3CCL2OH	0.0797
C10 Aromatics	C10H14H	NC9H20	0.0792
Methyl pyrrole isomers + Pentene nitrile isomers	C5H7NH	ME2BUT1ENE	0.0743
C6 esters	C6H12O2H	EMPHCOME	0.0690
Benzonitrile	C7H5NH	MC6OTKETOH	0.0685
Thiophene	C4H4SH	IBUTOL	0.0610
2-methyl pyridine + 3-methylpyridine	C6H7NH	MIPK	0.0603
Dihydronaphthalene	C10H10H	C108NO3	0.0574
Dihydropyrrole + butane nitrile	C4H7NH	CL12PRCHO	0.0570
Methyl naphthalene	C11H10H	C129CO	0.0552
Propiolic acid	C3H2O2H	ALLYLOH	0.0542
Methyl chavicol (estragole)	C10H12OH	PINAL	0.0522
Ethylcyclopentanone	C7H12OH	HM33C4OH	0.0497
1,3-dimethylnaphthalene	C12H12H	NC1313OH	0.0493
Indene + propynyl benzene isomer	C9H8H	BPINENE	0.0488
4-pyridinol	C5H5NOH	TBUACET	0.0427
Camphor + other oxygenated monoterpenes	C10H16OH	C828PAN	0.0396
2-ethenyl benzofuran	C10H8OH	NOPINAOH	0.0379

2,5-dimethyl pyrrole + 1-ethylpyrrole + other C2 substituted pyrroles	C6H9NH	CYHXONAOOH	0.0366
Ethenamine	C2H5NH	C2H6	0.0346
Nitrobenzene	C6H5NO2H	ACECOCOCH3	0.0325
Pentanenitriles	C5H9NH	C5PAN6	0.0314
Phenylacetylene	C8H6H	MC6OTKETOH	0.0276
nitrotoluene	C7H7NO2H	ACCOPRONE	0.0246
dihydroxy pyridine + methyl maleimide	C5H5NO2H	M3PEAOH	0.0225
pyridine aldehyde + methylfuronitrile + nitrosobenzene	C6H5NOH	H25M2C6	0.0211
benzeneacetonitrile	C8H7NH	NC71CO	0.0207
C11 aromatics	C11H16H	C129CO	0.0197
ethylindene	C11H12H	BPINENE	0.0194
2-furancarbonitrile + 3-furancarbonitrile	C5H3NOH	H2M3C4CHO	0.0189
Trimethylamine	C3H9NH	MEPROPENE	0.0181
dimethyl pyridine + ethylpyridine + heptylnitriles	C7H9NH	M2PEDOH	0.0172
C7 acrylonitrile	C7H11NH	C6CO2OHPAN	0.0169
Acenaphthylene	C12H8H	DDEC3ONE	0.0164
Propene amine	C3H7NH	PXYL	0.0158
Cineole + other oxygenated monoterpenes	C10H18OH	HO36C10	0.0137
C12 aromatics	C12H18H	C126CHO	0.0113
4-methylpentanenitrile	C6H11NH	MPRK	0.0109
Carbon suboxide	C3O2H	EOX2COMEOH	0.0104
Methyl benzeneacetonitrile	C9H9NH	C920PAN	0.0104
Dimethyl disulfide	C2H6S2H	PXYCATECH	0.0098
C13 aromatics	C13H20H	BCKET	0.0097
butene nitrates	C4H7NO3H	NPRACBOOH	0.0078
Vinylpyridine	C7H7NH	THEX2ENE	0.0066
decanal	C10H20OH	NC11H24	0.0065
Nitrofuran	C4H3NO3H	MALDALCO3H	0.0064
Methanimine	CH3NH	C2H6	0.0062
Propiolonitrile (=propyne nitrile)	C3HNH	DICLETOH	0.0058
Butene amine	C4H9NH	MVK	0.0055
nitroethene	C2H3NO2H	PROPACID	0.0054
Ethylnylpyrrole	C6H6N	CYHXONAOOH	0.0046
methane diol	CH4O2H	ETHOXOOH	0.0041
Nitroethane or ethane nitrite	C2H5NO2H	ETHOX	0.0035
Ethylamine + dimethylamine	C2H7NH	CRESOL	0.0030
Dihydro pyridine	C8H9NH	C5PAN6	0.0029
Nitropropanes	C3H7NO2H	PROPACID	0.0018
Cyanoallene isomers	C4H3NH	IPECOH	0.0013
C8 nitriles	C8H15NH	HEPT3ONE	0.0012
Dimethyl trisulfide	C2H6S3H	PXYCATECH	0.0011
n-sulfinyl methanamine	CH3NOSH	C2H6	0.0003

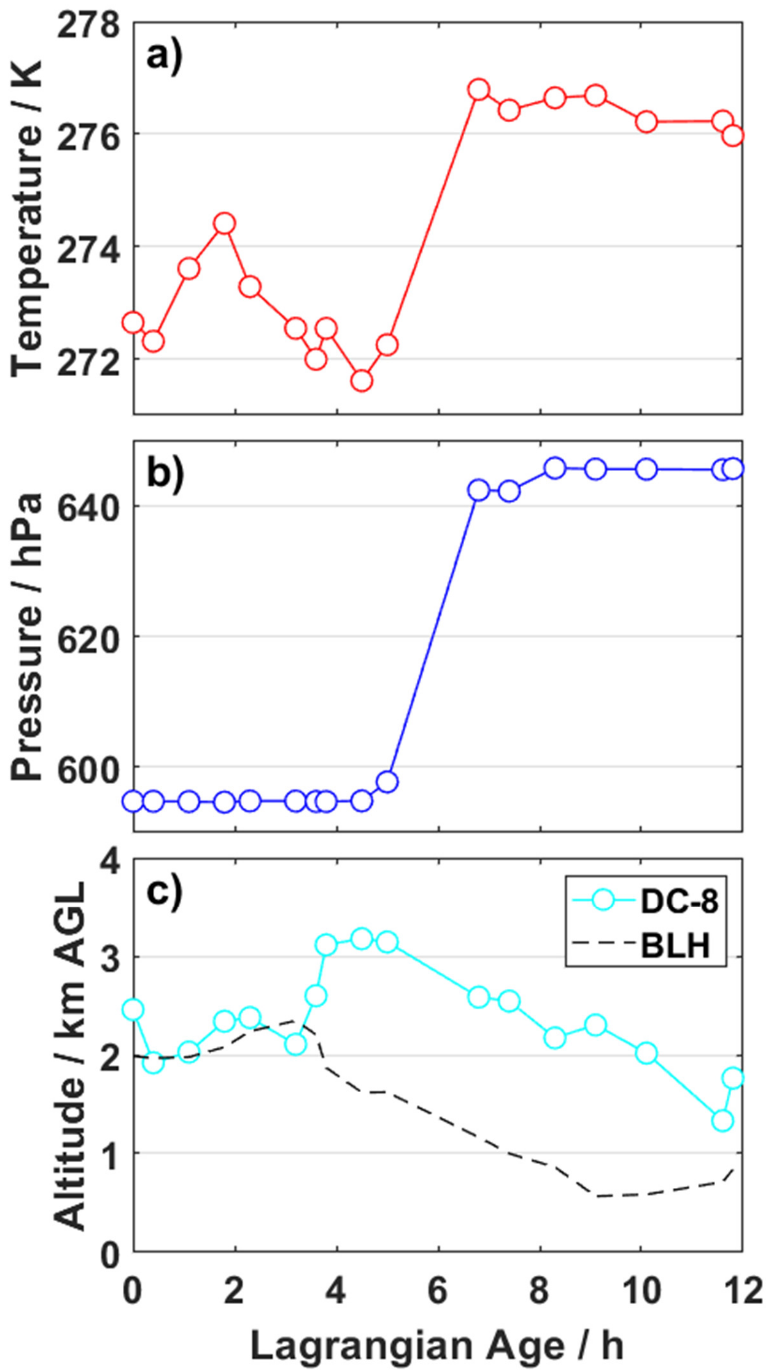

Figure S1. DC-8 sampling temperature (a), atmospheric pressure (b), and altitude above ground level (c, cyan circles) as a function of plume Lagrangian Age. The dashed line in (c) denotes the boundary layer height relative to ground level based on output from the two meteorological datasets used for trajectory analysis.

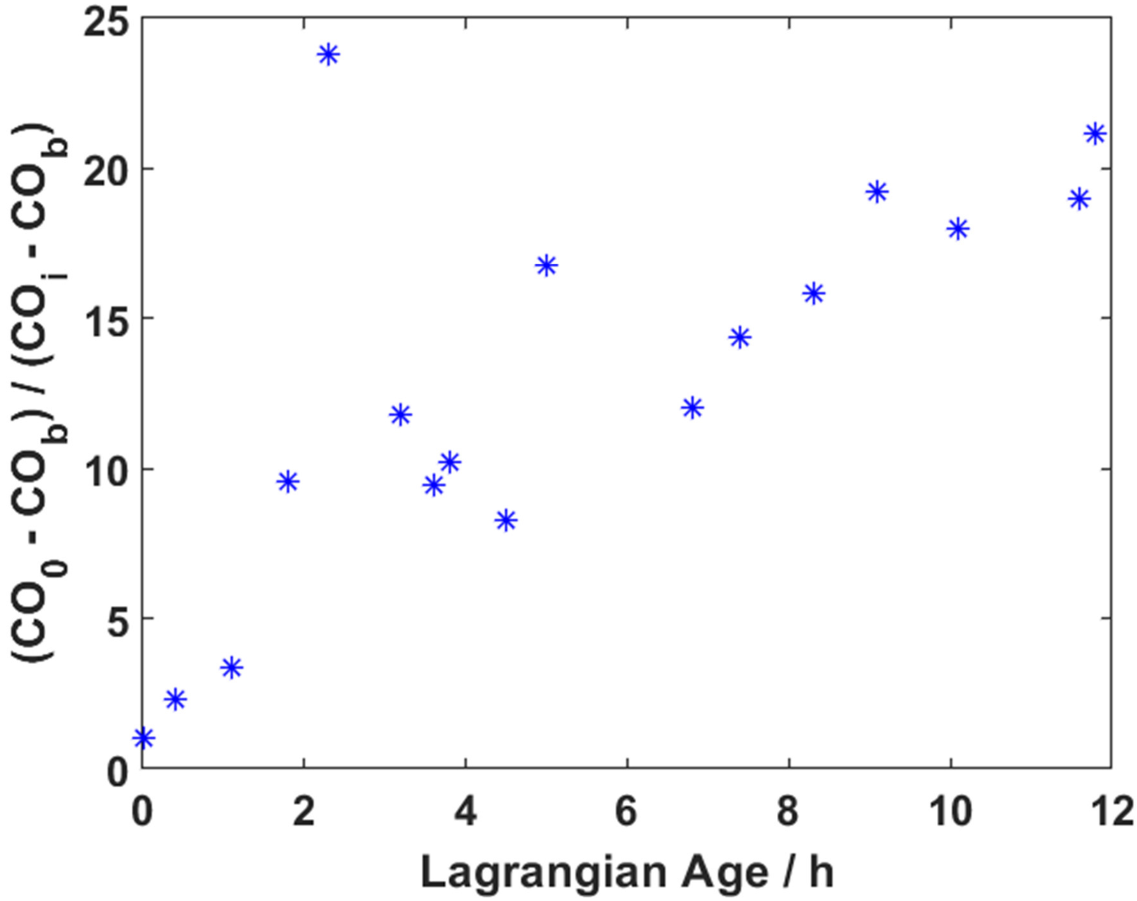

Figure S2. Dilution factor for each WAS plume sample, calculated as the ratio of initial to sample-time background-corrected CO.

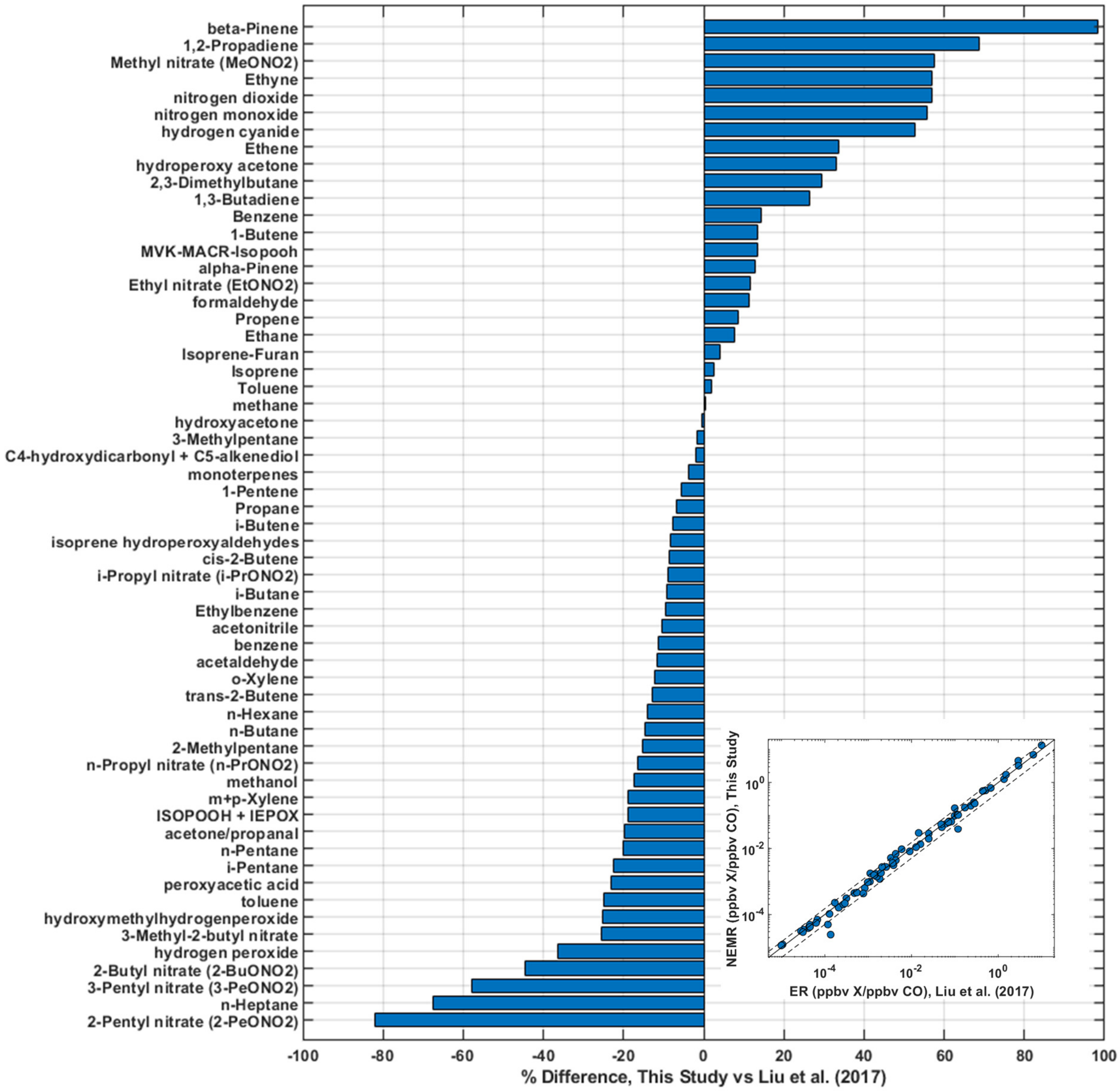

Figure S3. Comparison of normalized excess mixing ratios (NEMR) from the "source" sample of this study and the Rim Fire emission ratios (ER) reported by Liu et al. (2017). Both NEMR and ER values are normalized to excess CO. In the species-specific plot, positive values correspond to species with a higher ratio in long-axis source sample, and values with ER < 10^{-4} ppbv / ppbv are excluded. In the inset, the solid line is the 1:1 relationship and dashed lines are ±50%.

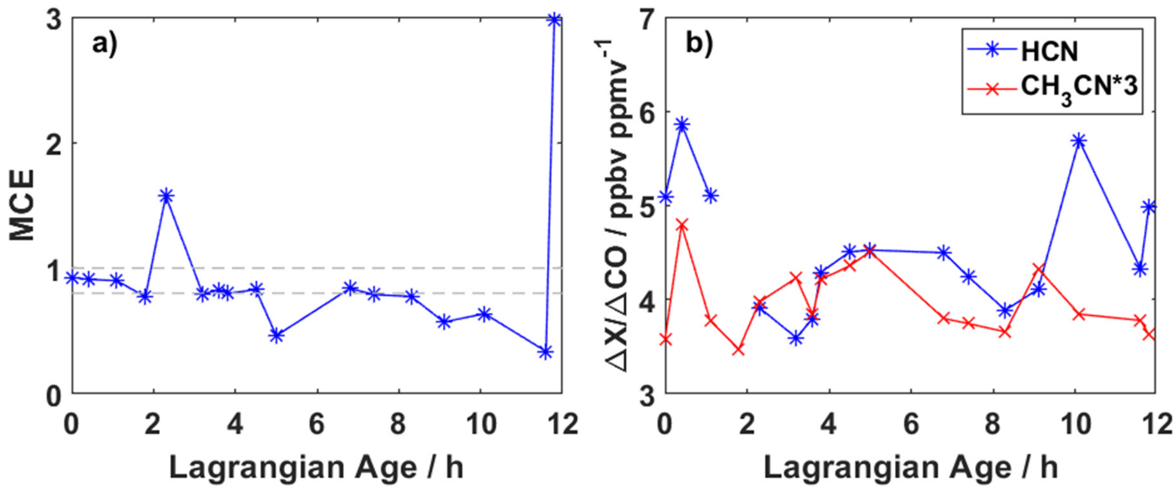

Figure S4. Modified combustion efficiency (MCE) (a) and NEMRs for formonitrile and acetonitrile (b). MCE is defined as ΔCO_2 / (ΔCO + ΔCO_2). Gray dashed lines in (a) denote the range of 0.8 – 1 typical of wildfires (Akagi et al., 2011).

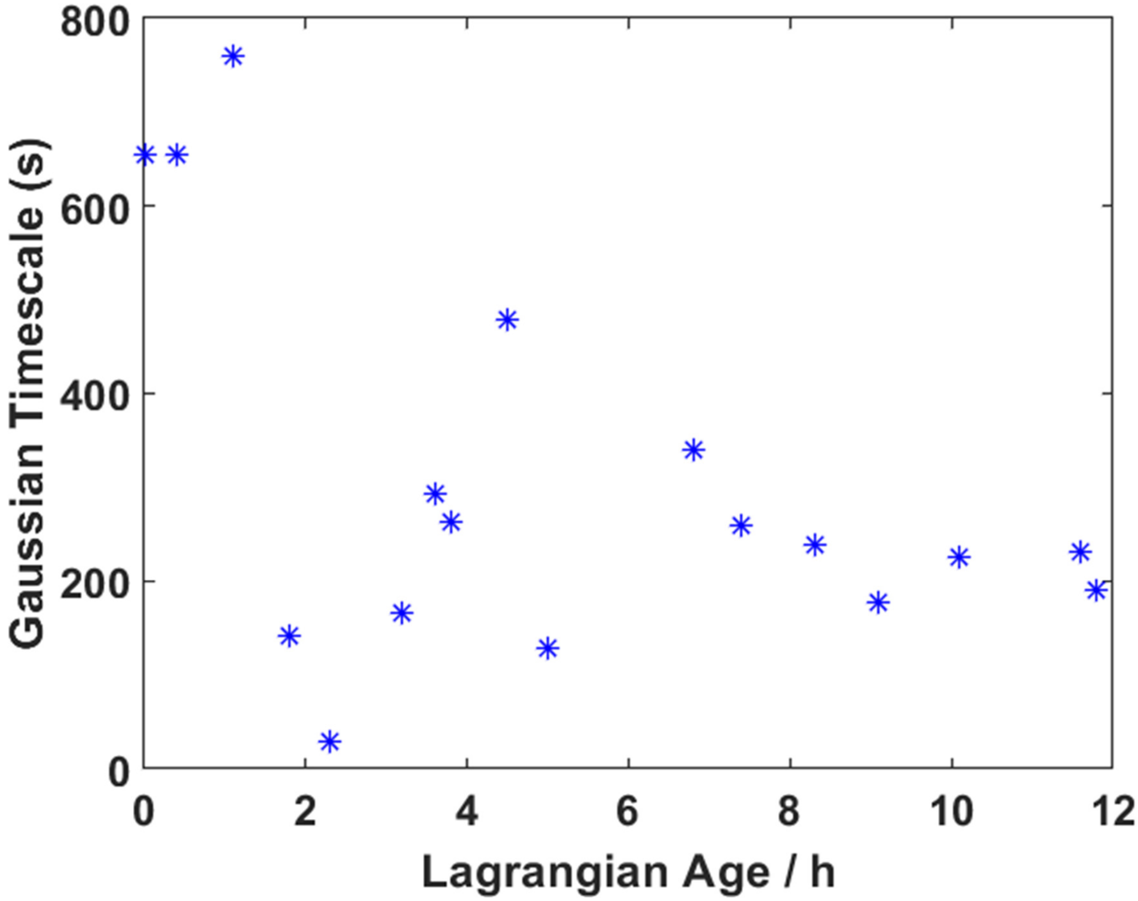

Figure S5. Gaussian dilution timescale for each model puff, calculated from observations of the decay of CO and Eqn. (2) as described in the main text.

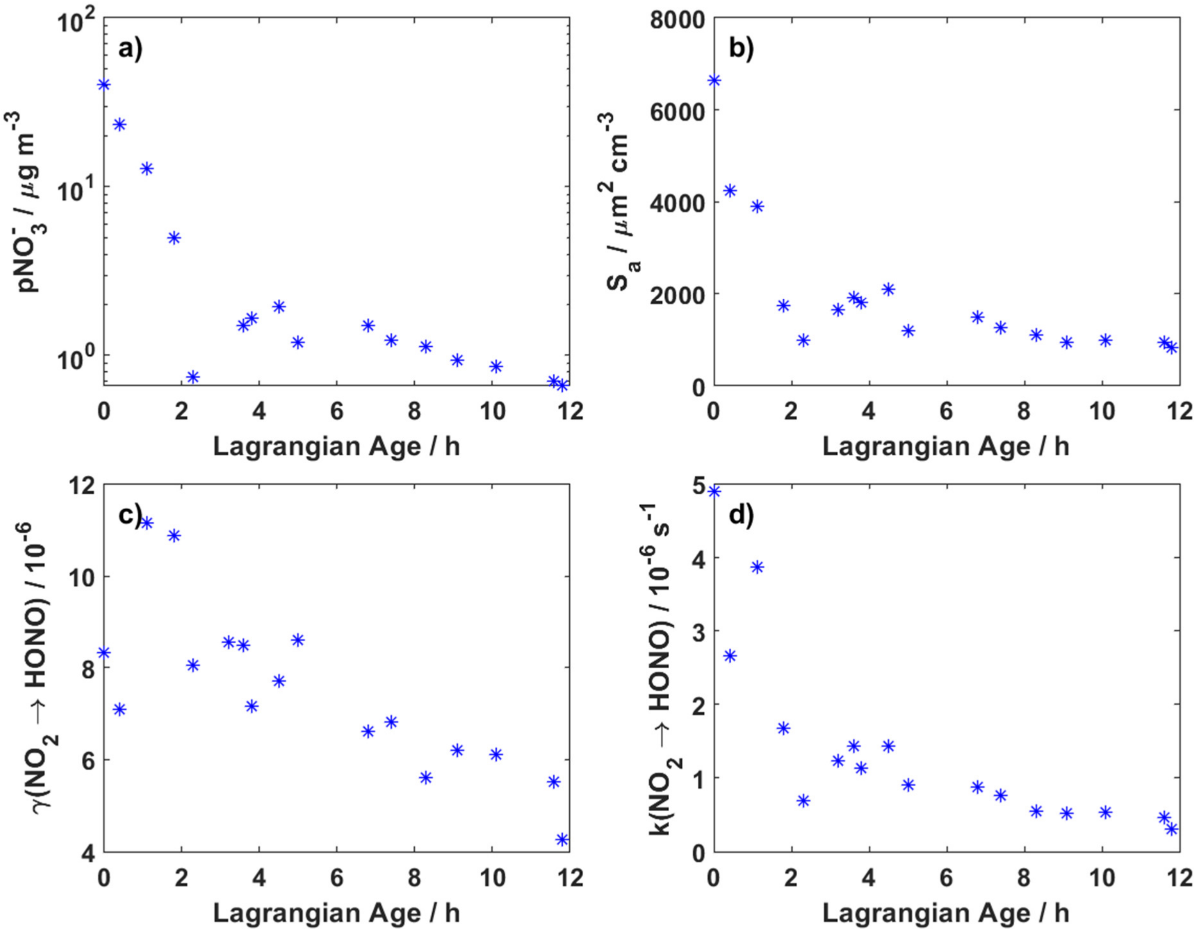

Figure S6. Observed and derived aerosol-related properties as a function of plume age: AMS-observed particulate nitrate mass concentration (a), LAS-observed aerosol surface area (b), calculated reactive uptake coefficient for NO_2 conversion to HONO (c), and calculated first order rate coefficient for the same (d).

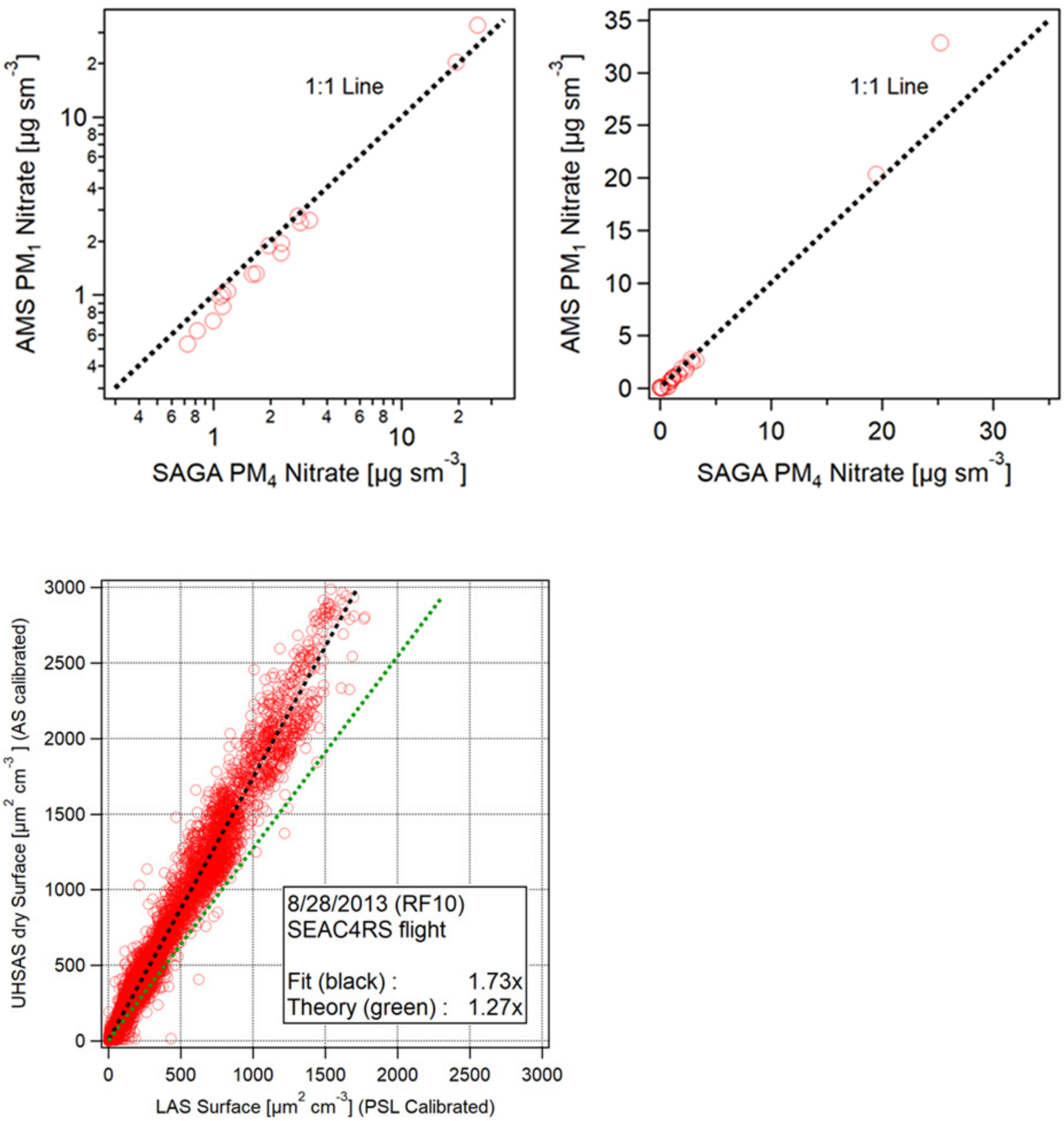

Figure S7. (top) Comparison of particulate nitrate observed by the AMS and SAGA instruments. The AMS has a size cut of ~1 micron, while SAGA samples up to 4 microns. AMS data are averaged over the SAGA sampling interval (~5 minutes) for all Rim Fire observations. Data is shown on both a log (left) and linear (right) scale. (bottom) Comparison of aerosol surface area observed by the LAS and UHSAS instruments. Low bias in the LAS results from the use of PSLs for size calibration instead of ammonium sulfate (P. Campuzano-Jost, personal communication, 2021).

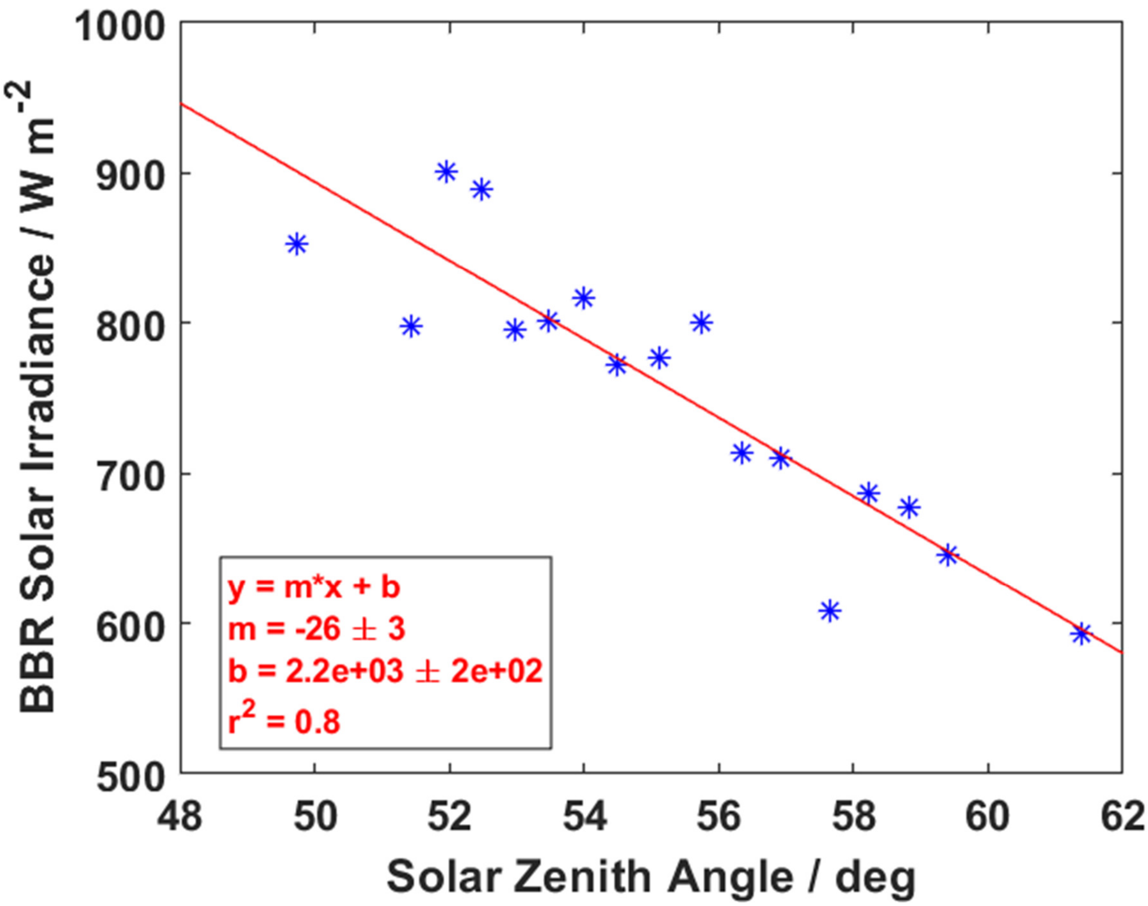

Figure S8. Linear relationship between solar zenith angle and total (up + down) solar irradiance from the broadband radiometer (BBR) instrument. The red line represents an ordinary least-squares fit, used to estimate irradiance for the parameterization of NO_2 reactive uptake.

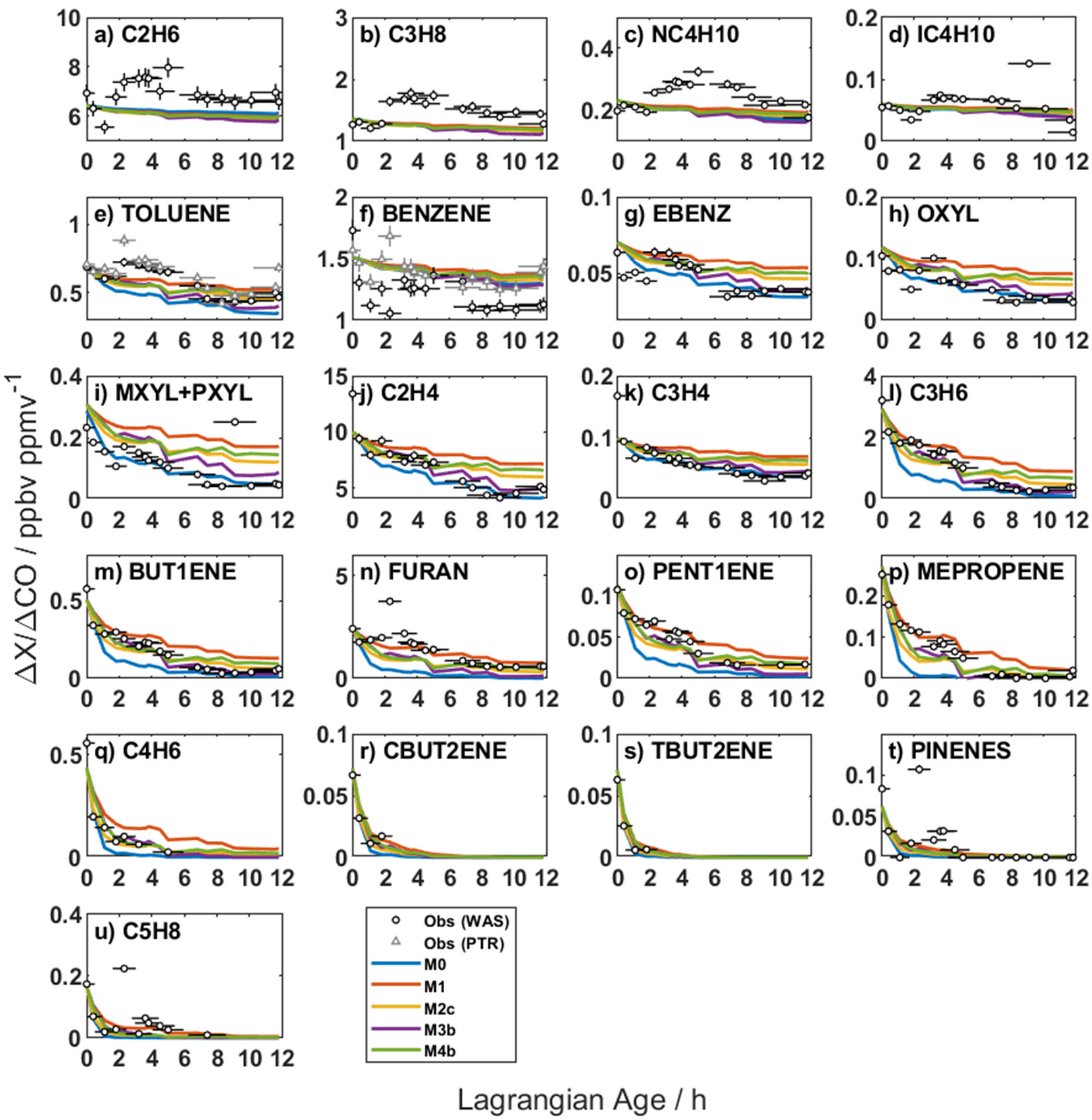

Figure S9. Age evolution of NEMRs for all observed VOC. Black circles and gray triangles are observations from the WAS and PTR-MS, respectively, with their corresponding uncertainty due to measurement accuracy and age. Species, in order from a) to u), are: ethane, propane, n-butane, i-butane, toluene, benzene, ethyl benzene, o-xylene, m-xylene + p-xylene, ethene, propadiene, propene, 1-butene, furan, 1-pentene, methyl propene (isobutene), 1,3-butadiene, cis-2-butene, trans-2-butene, α-pinene + β-pinene, and isoprene. Colored lines are model output from the base simulation (M0, blue), addition of unmeasured VOC (M1, red), and addition of unmeasured VOC and primary HONO (M2c, yellow) or secondary HONO via pNO_3^- photolysis (M3b, purple). Note that the furan observation is the difference between PTR-MS (furan + isoprene) and WAS isoprene.

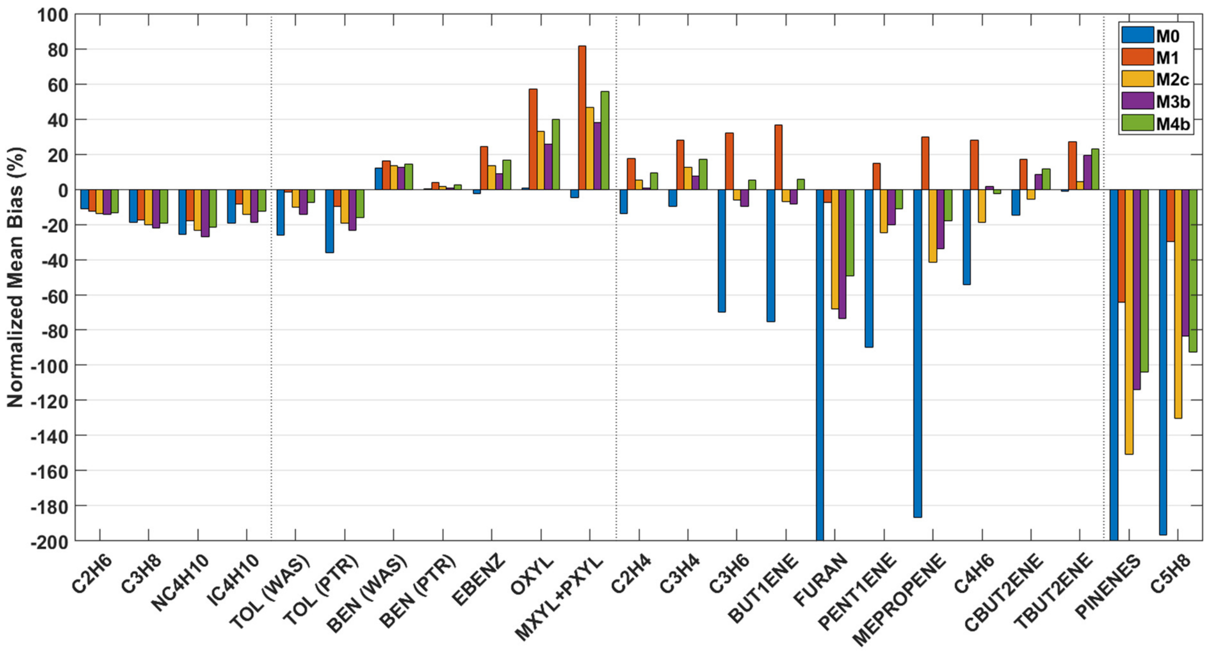

Figure S10. Normalized mean bias NMB modeled VOC profiles compared to observations. For each simulation and each VOC, NMB is computed with model output shown in the previous figure following (Gustafson and Yu, 2012). Negative bias means that the model is lower than observations, on average. Vertical dotted lines demarcate the four groups discussed in the main text.

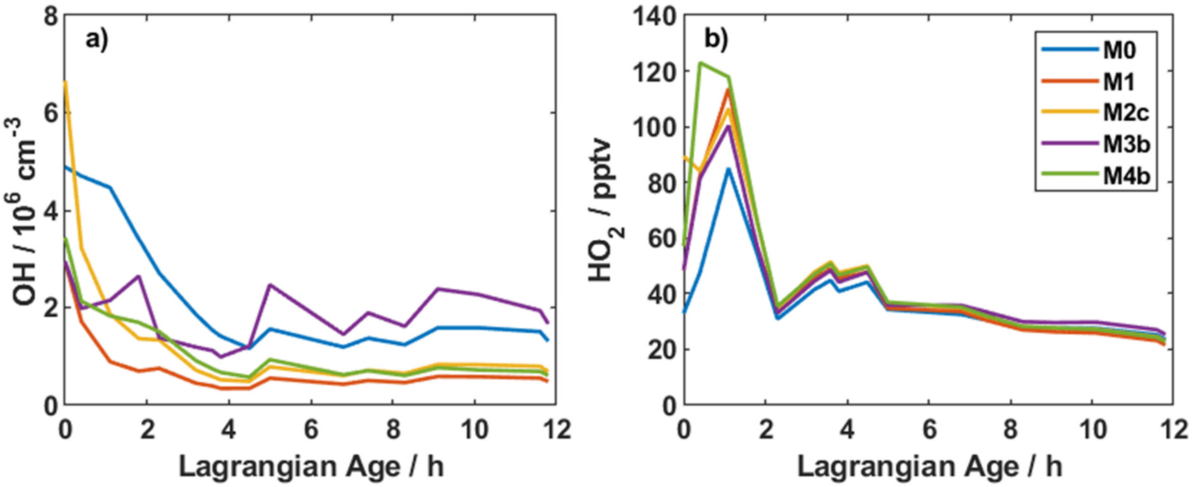

Figure S11. Age evolution of model-predicted OH concentration (a) and HO_2 mixing ratio (b). Colors are as described in Fig. S9.

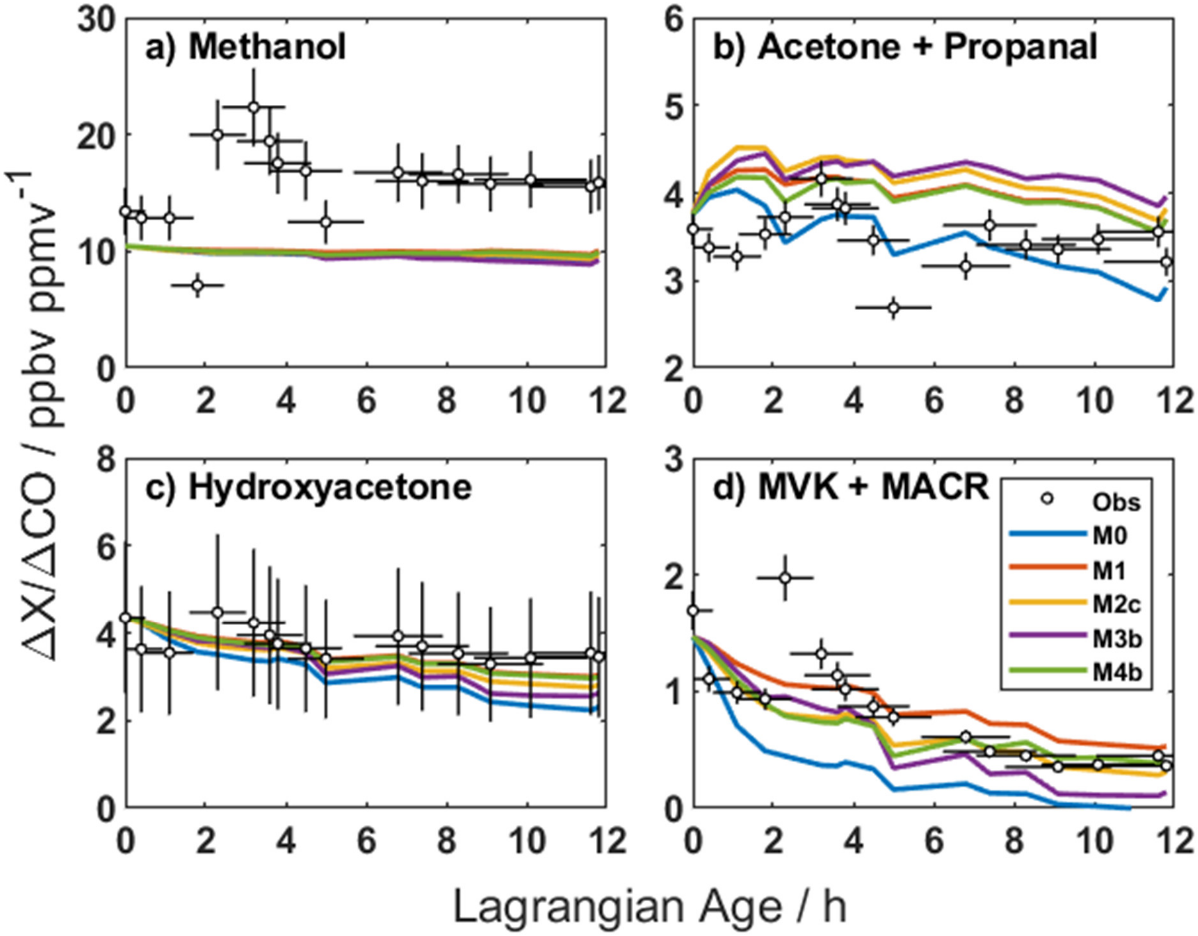

Figure S12. Age evolution of NEMRs for oxygenated VOC. Black circles are observations with their corresponding uncertainty due to measurement accuracy and age. Colored lines are as described in Fig. S9.

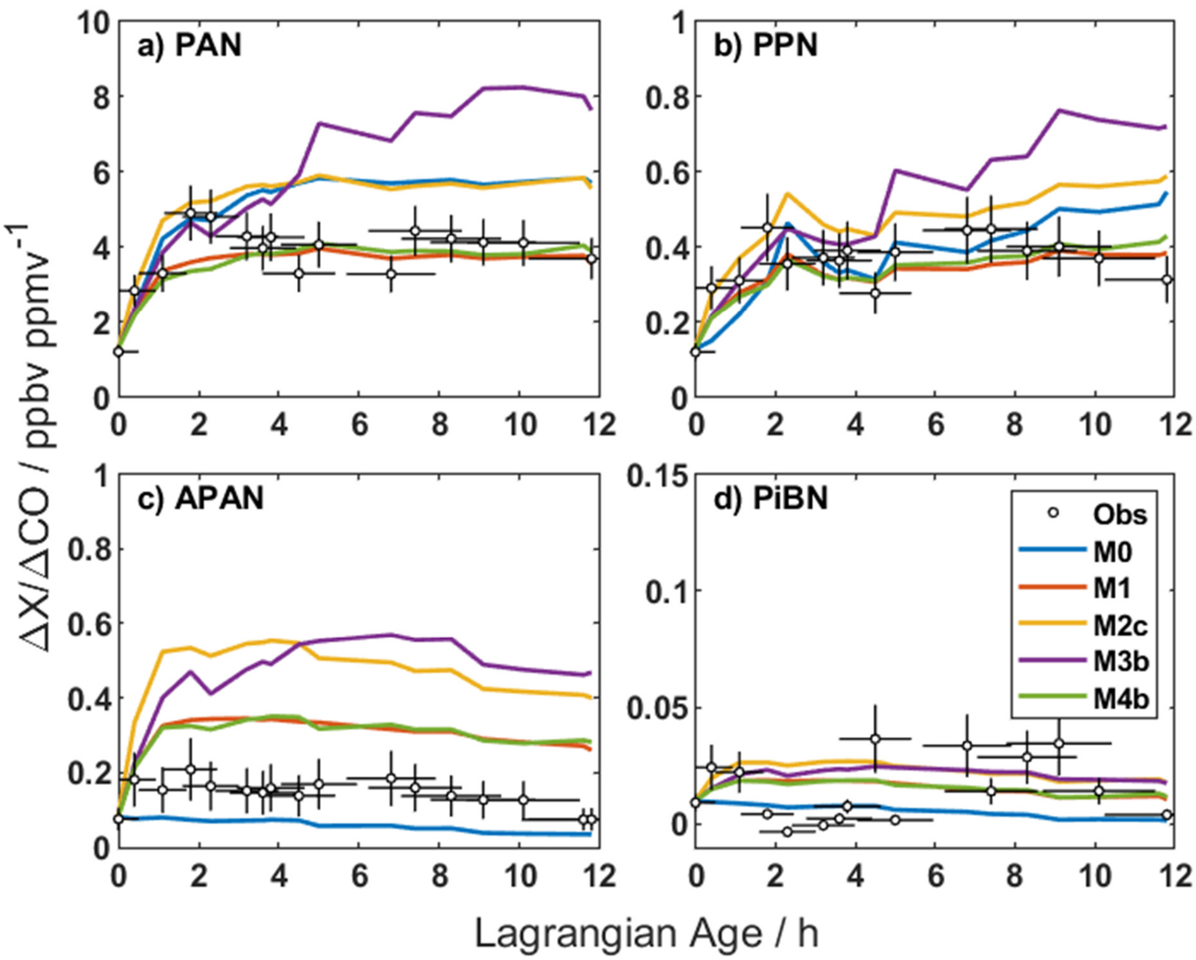

Figure S13. Age evolution of NEMRs for speciated peroxynitrates. Black circles are observations with their corresponding uncertainty due to measurement accuracy and age. Colored lines are as described in Fig. S9.

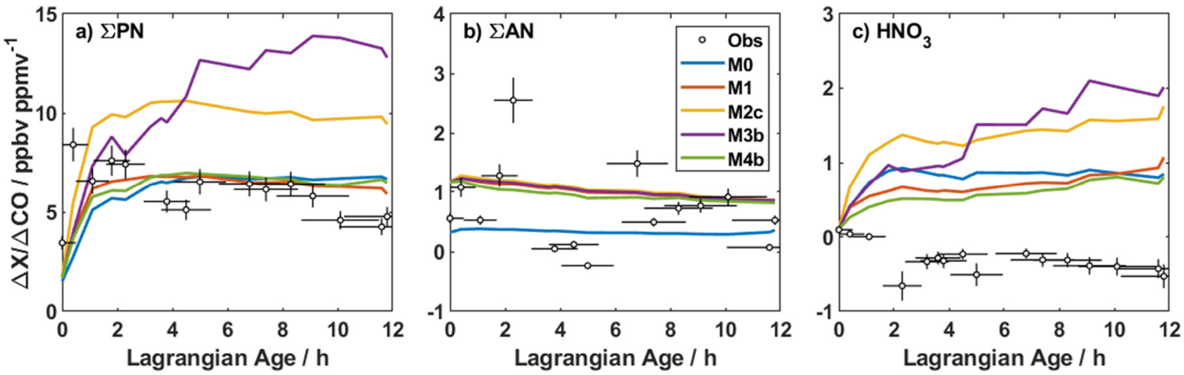

Figure S14. Age evolution of NEMRs for total peroxy nitrates (a), total alkyl nitrates (b), and nitric acid (c). Black circles are observations with their corresponding uncertainty due to measurement accuracy and age. Colored lines are as describe in Fig. S9. MCM PN and AN species are identified using simplified molecular-input line-entry system (SMILES) strings and SMILES filtering code provided with F0AM. Model HNO_3 NEMRs deviate significantly from observations because the model does not account for gas-to-particle nitrate partitioning.

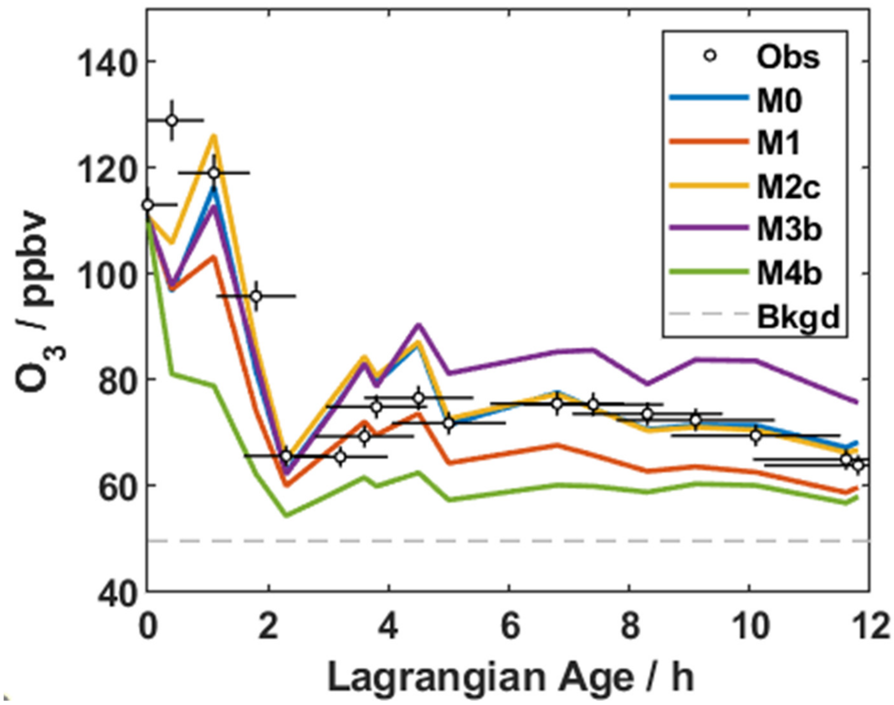

Figure S15. Age evolution of absolute ozone mixing ratio. Symbols and lines are as described Fig. S9. The grey dashed line denotes the estimated O_3 background mixing ratio.

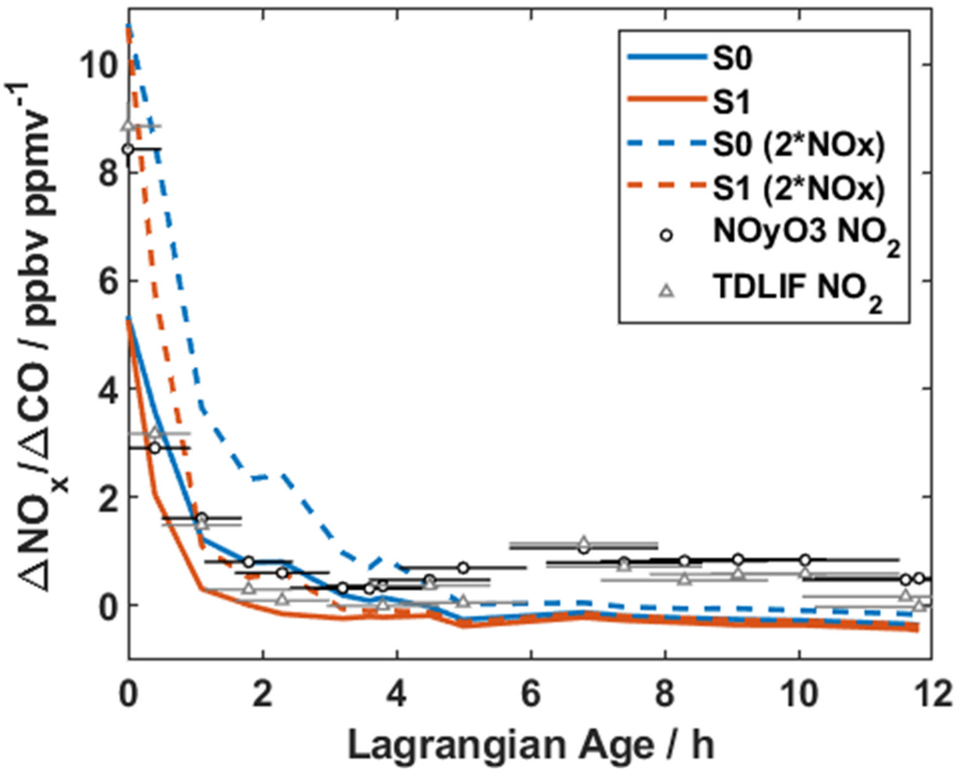

Figure S16. Comparison of NO_x NEMRS for observations (symbols), simulations M0/M1 (solid lines), and sensitivity perturbations where initial NO_x is doubled (dashed lines). For observations, black circles and gray triangles represent NO_x calculated with two different NO_2 measurements and the same NO measurement (from the NOyO3 instrument). Error bars denote uncertainty due to age estimation. Uncertainty due to measurement accuracy is small (4%).

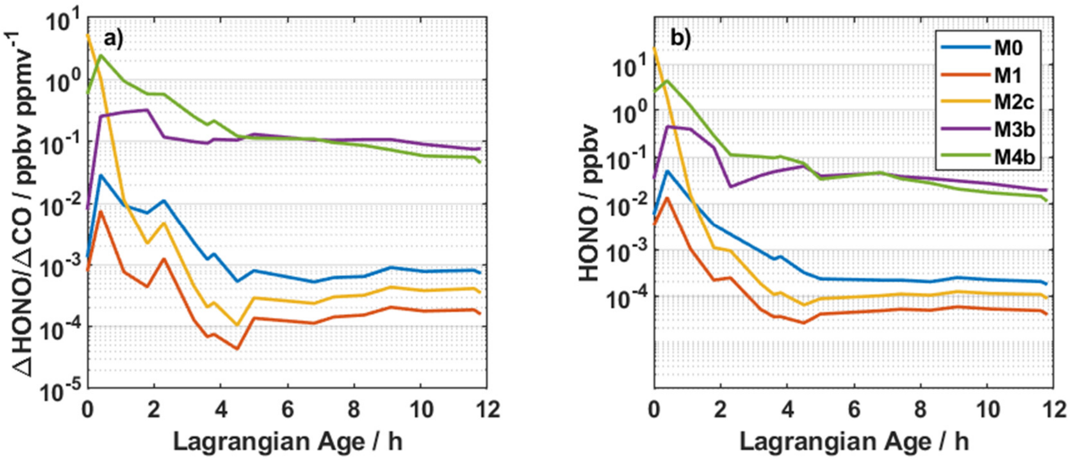

Figure S17. Age evolution of simulated HONO NEMRs (a) and absolute HONO mixing ratios (b). Colored lines are as described in Fig. S9.

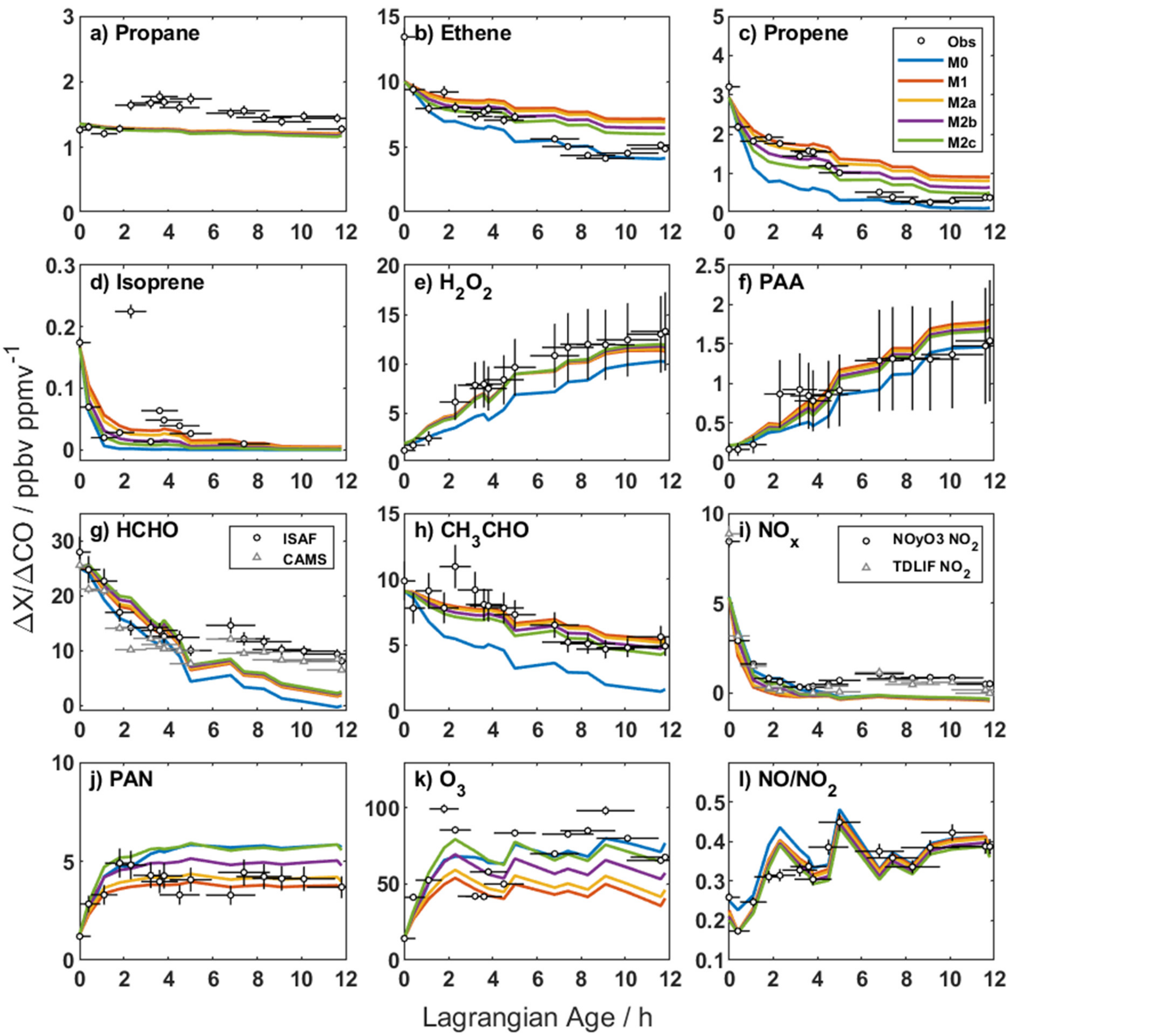

Figure 18. Age evolution of NEMRs for sensitivity simulations to assumed initial HONO concentration. Black circles are observations with their corresponding uncertainty due to measurement accuracy and age. Colored lines are model output from the base simulation (M0, blue), addition of unmeasured VOC (M1, red), and addition of unmeasured VOC plus primary HONO at mixing ratios of 5, 15, and 25 ppbv (yellow, purple, and green, respectively).

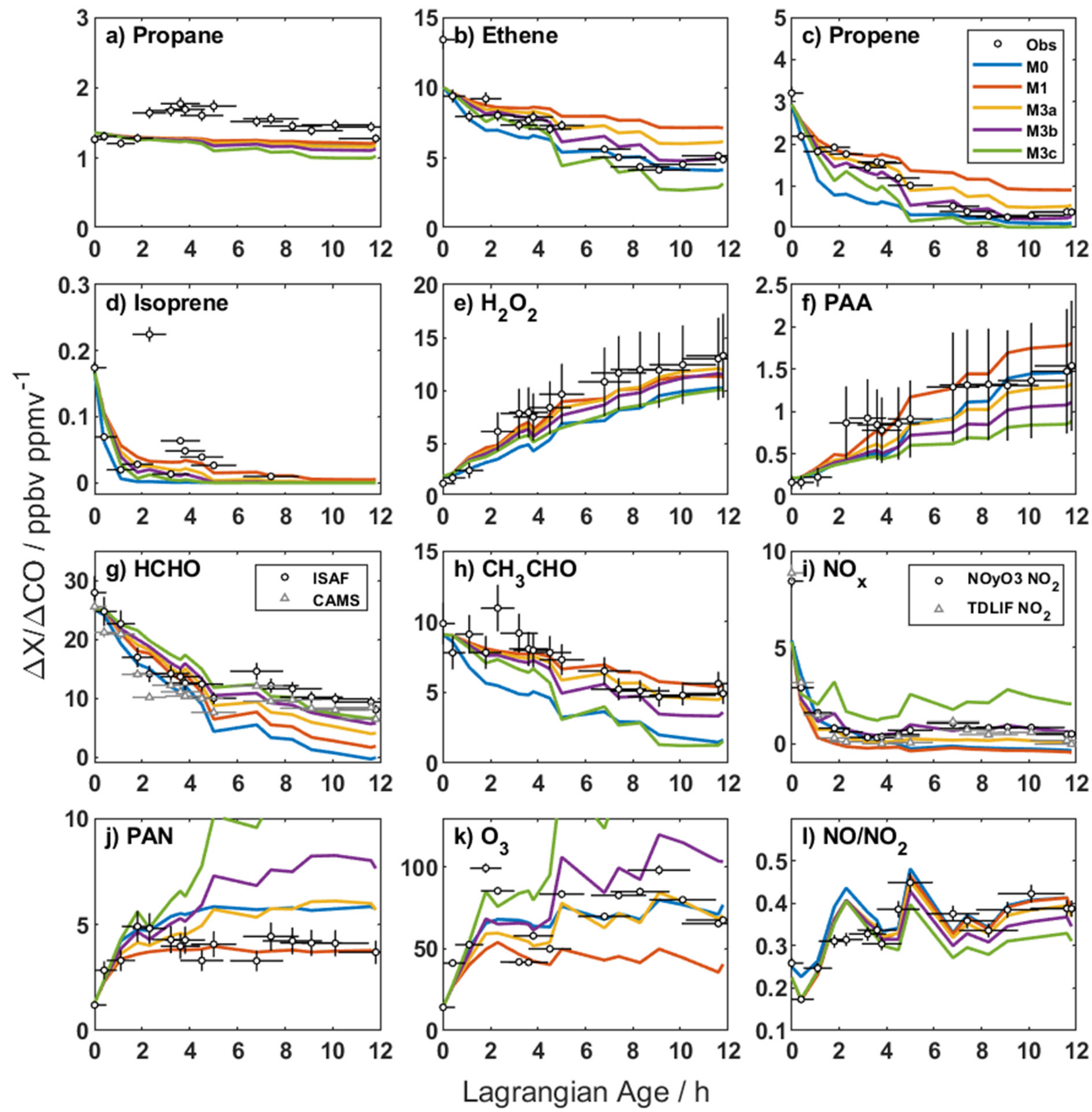

Figure 19. Age evolution of NEMRs for sensitivity simulations to particulate nitrate photolysis. Black circles are observations with their corresponding uncertainty due to measurement accuracy and age. Colored lines are model output from the base simulation (M0, blue), addition of unmeasured VOC (M1, red), and addition of unmeasured VOC plus pNO_3^- photolysis with rate multipliers of 0.5, 1, and 2 (yellow, purple, and green, respectively). See Sect. 2.4.2 and Table 1 in the main text for further details.

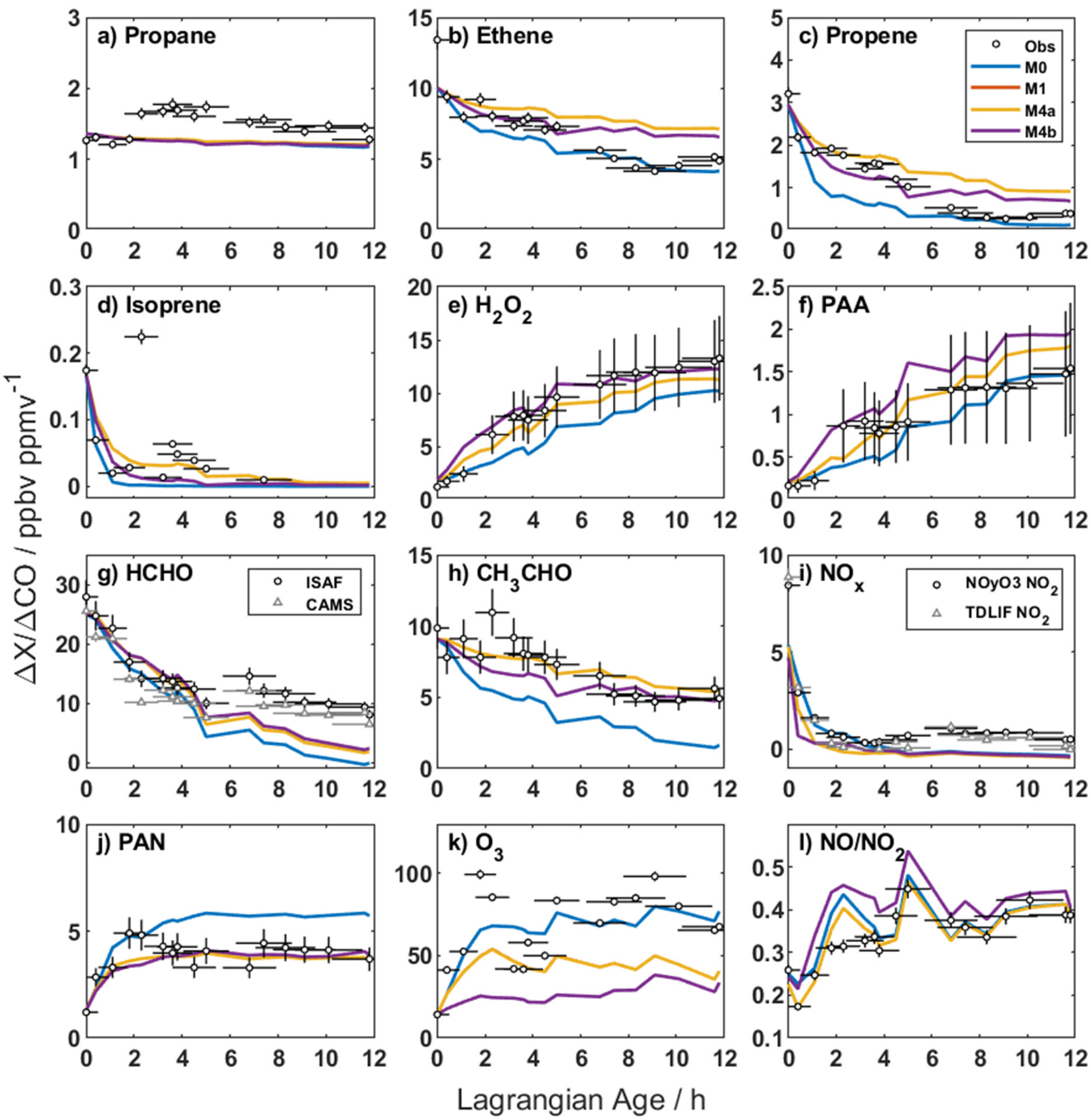

Figure 20. Age evolution of NEMRs for sensitivity simulations to heterogeneous reaction of NO_2. Black circles are observations with their corresponding uncertainty due to measurement accuracy and age. Colored lines are model output from the base simulation (M0, blue), addition of unmeasured VOC (M1, red), and addition of unmeasured VOC plus NO2 heterogeneous reaction with rate multipliers of 1 and 1000 (yellow and purple, respectively). See Sect. 2.4.2 and Table 1 in the main text for further details. Note that there is no visible difference in model output for simulations M1 and M4a.

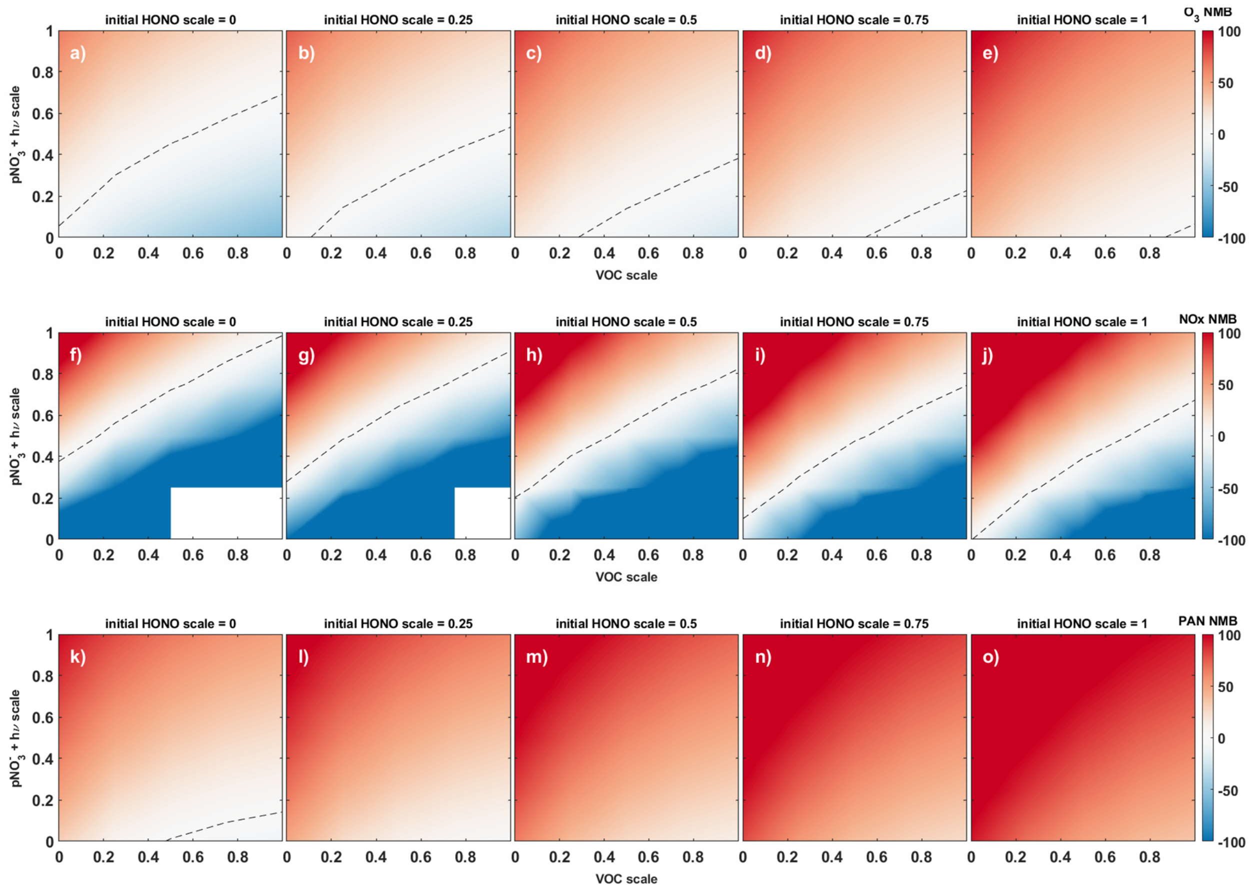

Figure S21. NMB of NEMRs for ozone (a-e), NOx (f-j), and PAN (k-o) for the sensitivity simulations described in Sect. 2.4.3 and Sect. 3.4. Simulations involve iteratively scaling unmeasured VOC (x-axis), pNO3- photolysis (y-axis), and initial HONO (columns) by factors of 0, 0.25, 0.5, 0.75, and 1. Shading indicates NMB of simulation NEMRs against observations, ranging from negative (blue) to positive (red) values. Dashed lines indicate interpolated contours for NMB of zero, corresponding to values shown in Figs. 5 and S22.

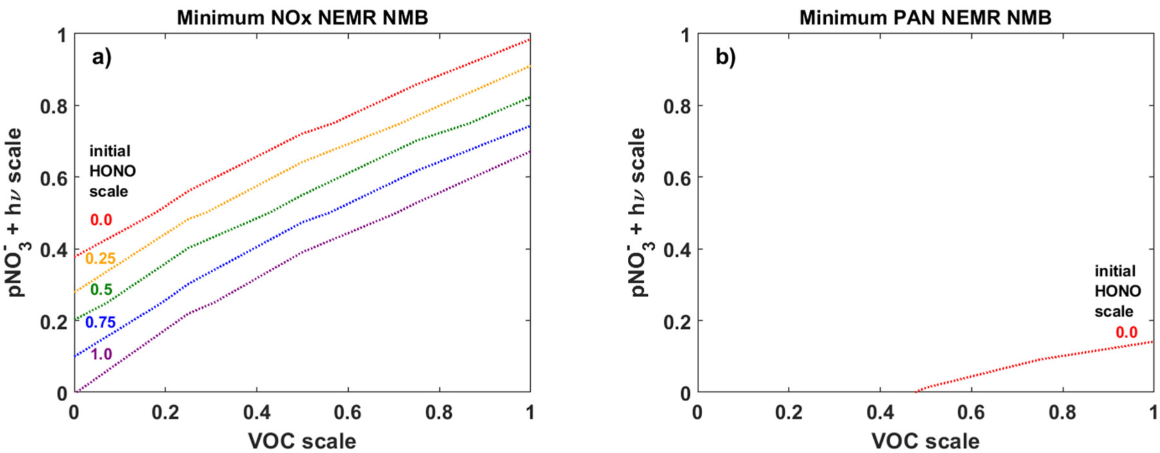

Figure S22. Isopleths for net-zero values of the normalized mean bias (NMB) for NEMRs of NO_x (a) and PAN (b). Each colored dotted line represents a fixed scaling factor for initial HONO mixing ratios. The x-y coordinates for a point on a given line represent a combination of VOC and pNO_3^- photolysis scaling factors that minimize the O_3 NEMR NMB. Isopleths are based on interpolation of results from the optimization simulations (Fig. S21).

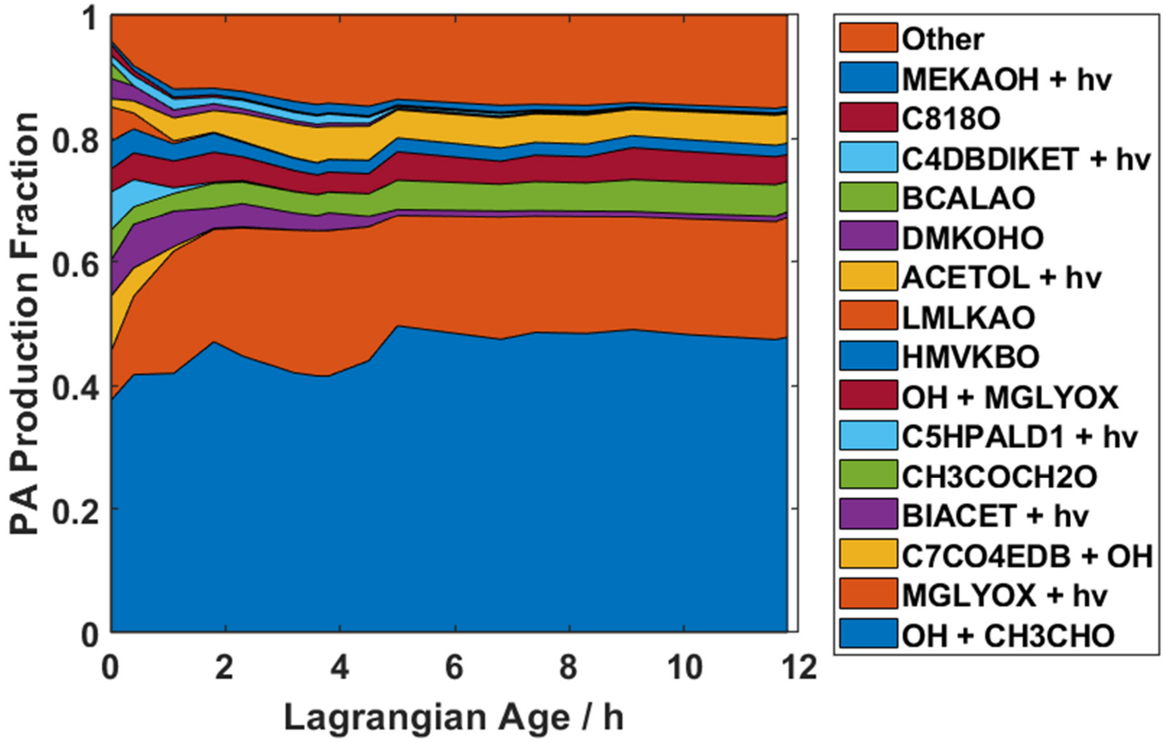

Figure S23. Fractional contributions to production of peroxyacetyl radical in simulation M3b.